Environmental Science & Technology

pubs.acs.org/est

Article

Mechanisms of Thermal Decomposition in Spent NCM Lithium-Ion Battery Cathode Materials with Carbon Defects and Oxygen Vacancies

Kang Liu, Zibo Xu, Mengmeng Wang, Daniel S. Alessi, Yuanzhi Tang, and Daniel C. W. Tsang*

Cite This: *Environ. Sci. Technol.* 2024, 58, 21362−21373

Read Online

ACCESS | Metrics & More | Article Recommendations | Supporting Information

ABSTRACT: Resource recovery from retired electric vehicle lithium-ion batteries (LIBs) is a key to sustainable supply of technology-critical metals. However, the mainstream pyrometallurgical recycling approach requires high temperature and high energy consumption. Our study proposes a novel mechanochemical processing combined with hydrogen (H_2) reduction strategy to accelerate the breakdown of ternary nickel cobalt manganese oxide (NCM) cathode materials at a significantly lower temperature (450 °C). Particle refinement, material amorphization, and internal energy storage are considered critical success factors for the accelerated decomposition of NCM cathode materials. In our proposed approach, NCM cathode materials can develop active sites with carbon defects (C_v) and oxygen vacancies (O_v), which improve the reduction and breakdown of H_2. The adsorbed H_2 on the surface of NCM decomposes into H* and combines with oxygen to form OH species, which can be facilitated by O_v *via* the enhanced charge transfer. The introduced C_v can enhance H_2 cracking and generate *C−H species to promote the thermal decomposition of NCM. The presence of defects proves to foster the preferential reduction of Mn(IV) by H_2, leading to a lower activation energy for the NCM decomposition (from 139 to 110 kJ/mol) with less H_2 consumption. Life cycle assessment suggests a reduction of 4.42 kg CO_2 eq for the recycling of every 1.0 kg of retired batteries. This study can promote material circularity and minimize the environmental burden of mining technology-critical metals for a low-carbon transition.

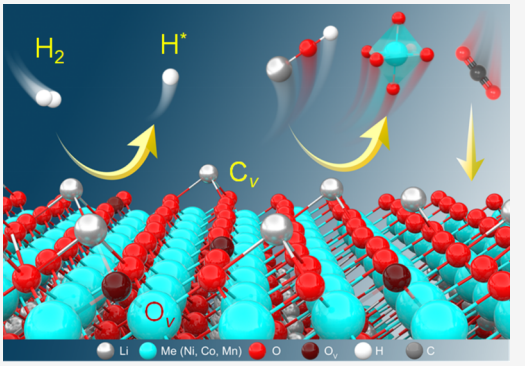

KEYWORDS: *hydrogen metallurgical treatment, battery waste recycling, oxygen vacancy, carbon defect, thermochemical decomposition, sustainable waste management*

1. INTRODUCTION

Lithium-ion batteries (LIBs), constituting 40 to 60% of the total costs of an electric vehicle, play a critical role in clean energy infrastructure for reducing carbon emissions.[1−4] Establishing closed-loop circulation and efficient material flow channels for the technology-critical metals (*e.g.*, Li, Co, Ni, and Mn) in battery materials emerges as an imperative strategy to ensure the security of material supply and overall sustainability of electric vehicle production.[5,6] Current techniques for recycling spent LIBs include pyrometallurgical processing,[7,8] hydrometallurgical extraction,[9,10] and direct material regeneration,[11,12] all of which can facilitate the closed-loop circulation of technology-critical metals for a sustainable industrial supply chain.[13,14] The requirements for carbon neutrality and circular economy have also increased the urgency of low-carbon recycling of technology-critical metals.[15,16]

Pyrometallurgical processing remains the most common technique for recycling cathode materials in spent LIBs.[17] However, the deconstruction process in carbothermal reduction metallurgical processing typically involves a high temperature of 700−1300 °C, owing to the high chemical stability of multicomponent lithium-containing crystals ($LiCoO_2$, $LiMnO_2$, and $LiNi_xCo_yMn_{1-x-y}O_2$).[12,18] Xiao et al. suggested that a temperature of 1400 °C can lead to the thermal decomposition of $LiCoO_2$, while the vacuum collapse of $LiMnO_2$ crystals requires a temperature over 700 °C.[19,20] The thermodynamic properties of lithium oxide escalate the required energy input for the battery recycling systems, resulting in higher recovery costs and increased risks of pollutant release.[21−23]

The EU Battery and Waste Battery Regulations, enacted in June 2023, require future electric vehicle batteries to include a carbon footprint statement and labeling to verify their low-carbon status.[24,25] As a critical link in the overall lifespan of batteries, how to minimize the carbon footprints in the

Received: July 1, 2024
Revised: October 23, 2024
Accepted: October 23, 2024
Published: November 1, 2024

https://doi.org/10.1021/acs.est.4c06562
Environ. Sci. Technol. 2024, 58, 21362−21373

recycling chain of battery materials is becoming an important focus of the electric vehicle industry.[26,27] The current research related to the recycling of retired LIBs focuses primarily on the separation of critical metals and the repair of cathode materials, while neglecting the associated environmental burdens and carbon emissions of these processes, which deserves necessary attention and further investigations.[28,29] Based on the aforementioned gaps in the field, our goal is to explore achieve a rapid and low-temperature cathode decomposition methods to close the loop on battery materials recycling.

This study proposes a low-carbon pyrometallurgical process that can rapidly decompose the ternary lithium nickel cobalt manganese cathode materials (hereafter referred to as NCM cathode materials) in spent LIBs at 450 °C to reduce reaction energy consumption and carbon emissions. Mechanochemical processing has been typically employed to facilitate hydrometallurgical reactions, but its effectiveness for pyrometallurgical reduction remains uncertain. Our study hypothesizes that mechanochemical processing can enhance the carbon defect (C_v) and oxygen vacancy (O_v) contents of NCM cathode materials, thereby promoting their breakdown and metal recovery during thermal reduction in an H_2 atmosphere. This study aims to: (1) validate the development of carbon defects and oxygen vacancies for promoting the low-temperature breakdown of NCM cathode materials; (2) combine density functional theory (DFT) calculation and experimental characterization to identify the predominant active sites (carbon defect and oxygen vacancy; C_v−O_v) for the reduction and decomposition of NCM cathode materials; and (3) evaluate the environmental contribution of C_v−O_v processing combined with H_2 reduction (C_v−O_v−H_2) to the thermal decomposition of NCM cathode materials *via* life cycle assessment for fostering a circular economy for battery recycling.

2. MATERIALS AND METHODS

2.1. Materials and Reagents. Retired ternary lithium nickel−cobalt−manganese (C/$LiNi_{0.5}Co_{0.2}Mn_{0.3}O_2$) power batteries were obtained from Xiaopeng New Energy Vehicle Company in Guangdong, China. The retired LIBs were first discharged in a homemade device and then crushed by a crusher to obtain cathode electrode material powder for experimental use. The sorted outer shell, aluminum foil, copper foil, and separator were recycled into new products separately. Table S1 presents the component weight of retired LIBs, and Table S2 details the metal contents. Ultrapure deionized water was used in the experiments. Nitric acid (AR, HNO_3, 68−70%) and hydrochloric acid (AR, HCl, 36−38%) from Aladdin Reagent Co., Ltd. were used for dissolving the NCM cathode material powder for composition analysis.

2.2. Experimental Methods. The experimental approach involved a synergistic combination of C_v−O_v with H_2 metallurgical processing for the recovery of Li from NCM cathode materials. Initially, 0.5 g of deactivated NCM cathode materials were placed into a zirconia planetary ball mill device (Deco Technology, Changsha, China) for mechanochemical processing at different rotational speeds (0, 200, 400, 600, and 800 rpm) for 1 h. A 0.1 g of the ball-milled NCM powder was loaded into a quartz boat and transferred into a tube furnace to initiate the H_2 reduction reaction under a He/H_2 (95/5; v/v) atmosphere. The use of mixed gas can reduce the concentration of H_2, for the sake of occupational safety of experimental and industrial processes. The tube furnace temperature was maintained at 350, 375, 400, 425, and 450 °C for 1 h, respectively. The cooled NCM cathode material reaction product was cleaned with a constant volume of deionized water, and the leaching solution was filtered through a 0.45 μm membrane (polyacrylonitrile fiber). The concentrations of metal ions in the filtrate were then measured using inductively coupled plasma optical emission spectroscopy (ICP-OES, Agilent 5110).

2.3. Characterization Methods. Crystalline phases in the samples were identified using X-ray diffraction (XRD) on a Rigaku Smart Lab instrument (Japan) at 10−80° 2θ with an X-ray voltage of 45 kV and a current of 200 mA. The scanning rate was 5°/min. The chemical state of elements on the solid samples' surfaces was analyzed by X-ray photoelectron spectroscopy (XPS) with an ESCALAB 250Xi spectrometer. The surface morphology of the products was analyzed using scanning electron microscopy with energy dispersive X-ray analysis (SEM-EDX) on a TESCAN VEGA3 XM instrument (Czech Republic). The weight loss and phase change of the material during heating was studied using thermogravimetry and differential scanning calorimetry (TG-DSC) on a PerkinElmer Pyris1 model instrument. High-resolution transmission electron microscopy (HR-TEM) and selected area electron diffraction (SAED) were conducted at 200 kV on a Titan G2 60−300 apparatus with an image corrector (FEI). Temperature Programmed Reduction (TPR-H_2) and Temperature Programmed Desorption (TPD-O_2) were measured using a temperature-programmed chemical adsorption analyzer (Micromeritics Auto Chem II 2920). An FEI Tecnai F30 instrument was used for high-resolution observation, aberration-corrected high-angle annular dark field-scanning transmission electron microscope (AC HAADF-STEM) imaging combined with Energy dispersive X-ray spectroscopy (EDS) analysis. The determination of oxygen vacancies was completed using electron paramagnetic resonance spectroscopy (E500, Bruker, Germany).

2.4. Density Functional Theory Calculation. Density functional theory calculation was conducted using the Vienna Ab initio Simulation Package (VASP).[30] Projected augmented waves (PAW) were used to characterize interactions between the core and valence electrons, and the generalized gradient approximation (GGA) based on the Perdew−Burke−Ernzerhof (PBE) exchange−correlation energy was used to characterize the local density.[31−34] Brillouin zone divisions were sampled utilizing the Monkhorst−Pack method. For the calculations, a cutoff energy value of 400 eV was chosen. The *k*-points were generated for dimensions ranging from 1 × 1 × 1 to 3 × 3 × 1 to optimize convergence sampling in computing the free energy and H_2 decomposition path. The convergence precision values were set at 1.0×10^{-4} eV for electron relaxation and 1.0×10^{-3} eV for ion relaxation. The force convergence criterion was determined at 0.02 eV/ Å.

2.5. Life Cycle Assessment. The environmental impacts of high-temperature decomposition of NCM cathode materials were systematically analyzed using a life cycle assessment (LCA) approach to evaluate the designed process, including (Route I) C-based metallurgical processing, (Route II) H_2 reduction metallurgical processing, and (Route III) C_v−O_v−H_2 reduction metallurgical processing.[35,36] The data sources for Routes I and II were from references and serve as comparisons for Route III. Life cycle environmental impacts were simulated using SimaPro 8.5 software developed by PRé Sustainability in The Netherlands. TRACI 2.1 V1.06/US 2008,

https://doi.org/10.1021/acs.est.4c06562
Environ. Sci. Technol. 2024, 58, 21362−21373

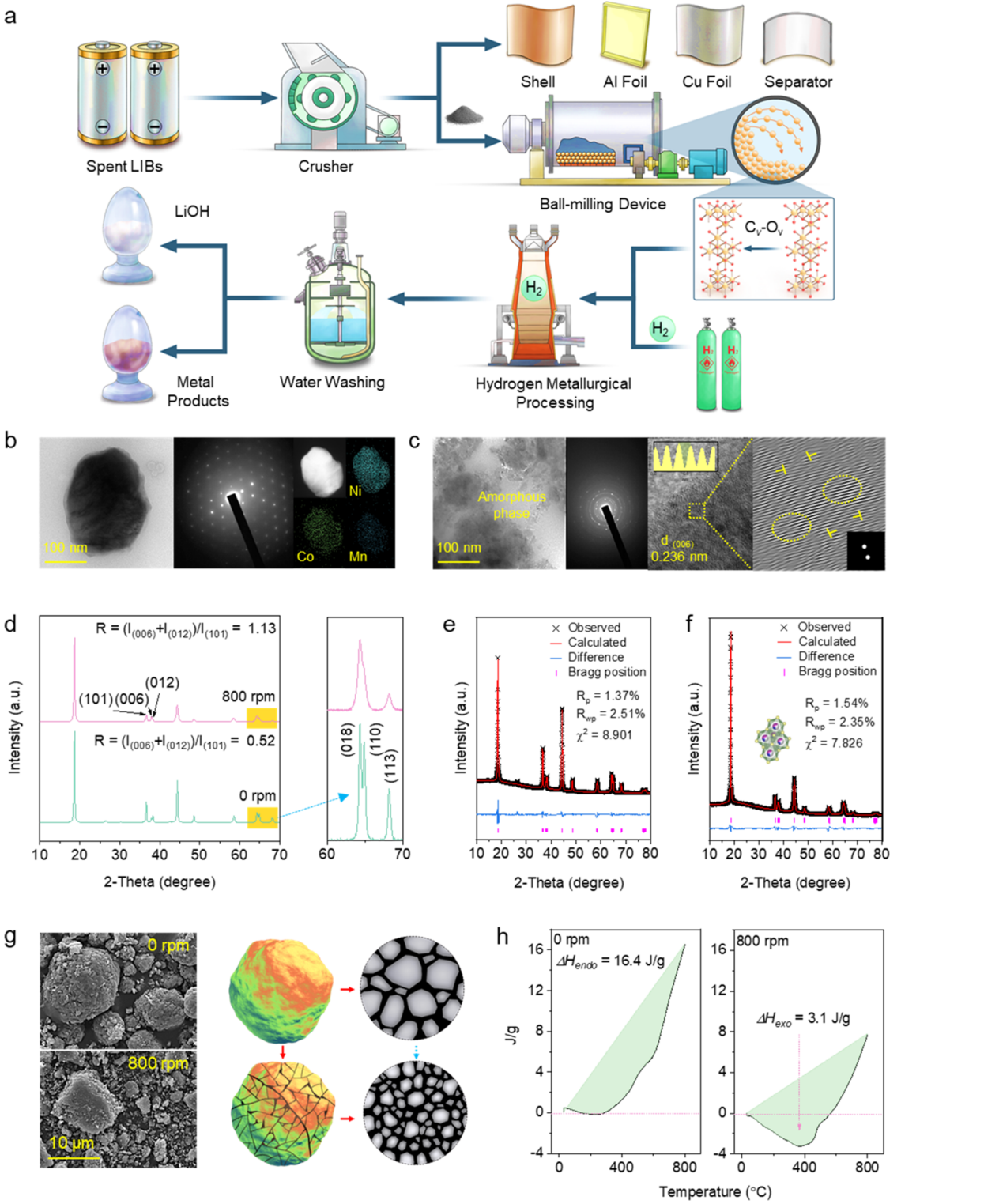

Figure 1. (a) Schematic illustration of the C_v−O_v combined and H_2 metallurgical processing for recycling the retired LIBs; characterization of NCM cathode materials: (b) HRTEM, SAED, and EDS mapping for pristine NCM cathode materials (defined as 0 rpm), (c) HRTEM and SAED for reacted NCM cathode materials (ball milled at 800 rpm), where yellow area shows the Fast Fourier Transform (FFT) changes in lattice spacing and enlarged fringes (scale of SEAD is 5 nm^{-1}); (d) XRD patterns of NCM cathode materials; (e, f) are XRD Rietveld refinement for unreacted and reacted NCM cathode materials, respectively; (g) SEM image and schematic illustration of the hypothesized structure changes in 3D; and (h) DSC curves and the corresponding internal energy reserves (0 and 800 rpm).

a widely used method for assessing chemical and environmental impacts, was employed to evaluate this procedure.[36] TRACI 2.1 provides an expanded assessment of factors that can cause potential effects, including global warming potential (GWP, kg CO_2 eq), fossil fuel depletion (FF, MJ surplus), ozone depletion (OD, kg CFC-11 eq), smog formation (PS, kg O_3 eq), acidification (AC, mol SO_2 eq), eutrophication (EU, kg N eq), carcinogenic effects (HHC, CTUh), noncarcino-

https://doi.org/10.1021/acs.est.4c06562
Environ. Sci. Technol. 2024, 58, 21362−21373

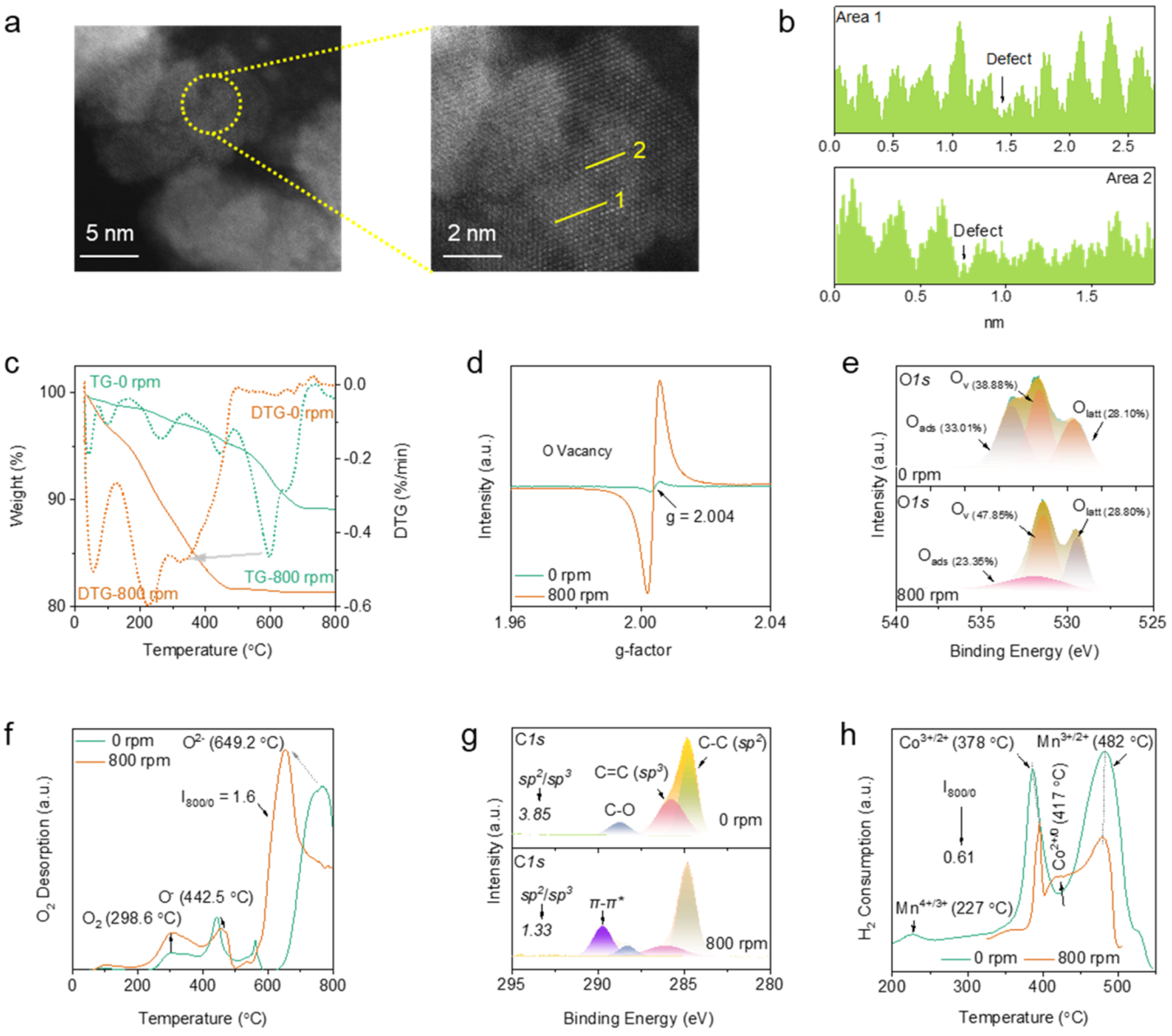

Figure 2. Characterization of NCM cathode materials before (0 rpm) and after (800 rpm) mechanochemical processing: (a) AC−HAADF−STEM, (b) measurement results of lattice spacing (Area 1 and 2), (c) TG−DTG (heat rate of 10 °C/min and N_2); (d) EPR; (e) high-resolution XPS results of O 1s, (f) O_2-TPD, (g) high-resolution XPS results of C 1s, and (h) H_2-TPR.

genic effects (HHNC, CTUh), respiratory effects (RE, kg PM 2.5 eq), and ecotoxicity (EC, CTUe).[37] The study utilized Ecoinvent 3 and the US Life Cycle Inventory (USLCI) databases as primary inventories to assess the environmental impacts from the beginning to the end of a product's life cycle. Detailed information, including boundaries (Figures S1−S3), material and energy flows (Tables S3−S5), and output LCA data (Tables S6−S8), are available in the Supporting Information (SI). Specifics of the calculation for the LCA data can be found in SI Texts S1−S6. The products recovered from spent NCM batteries are considered an alternative to materials manufactured in the market.

3. RESULTS AND DISCUSSION

3.1. Lattice Distortion and Internal Energy Storage.

Figure 1a shows a process diagram for our synergistic combination of C_v−O_v with H_2 metallurgical reduction for the low-temperature decomposition of NCM cathode materials. Typical single crystals of NCM cathode materials were observed under HRTEM and the structures were confirmed by SAED (Figure 1b). The homogeneous distribution of Ni, Co, and Mn was confirmed by EDX. After mechanochemical processing, the NCM single crystals were transformed into polycrystalline and amorphous phases as evidenced by HRTEM images and the corresponding SAED diffraction patterns (Figure 1c).[38,39] Detailed examination of the NCM lattices revealed distortion and disorder induced by mechanical forces (enlarged yellow area and circle). The XRD patterns (Figure 1d) indicated the merging and broadening of diffraction peaks on the (018), (110), and (113) crystal planes following mechanochemical processing, consistent with HRTEM−EDX−SAED observation on the transformation from well-ordered crystalline phase to less ordered/disordered state. The orderliness of layered materials can be assessed using the *R* factor: a lower *R*-value indicates better orderliness.[40] The *R* factor, calculated as the ratio of individual peak

https://doi.org/10.1021/acs.est.4c06562
Environ. Sci. Technol. 2024, 58, 21362−21373

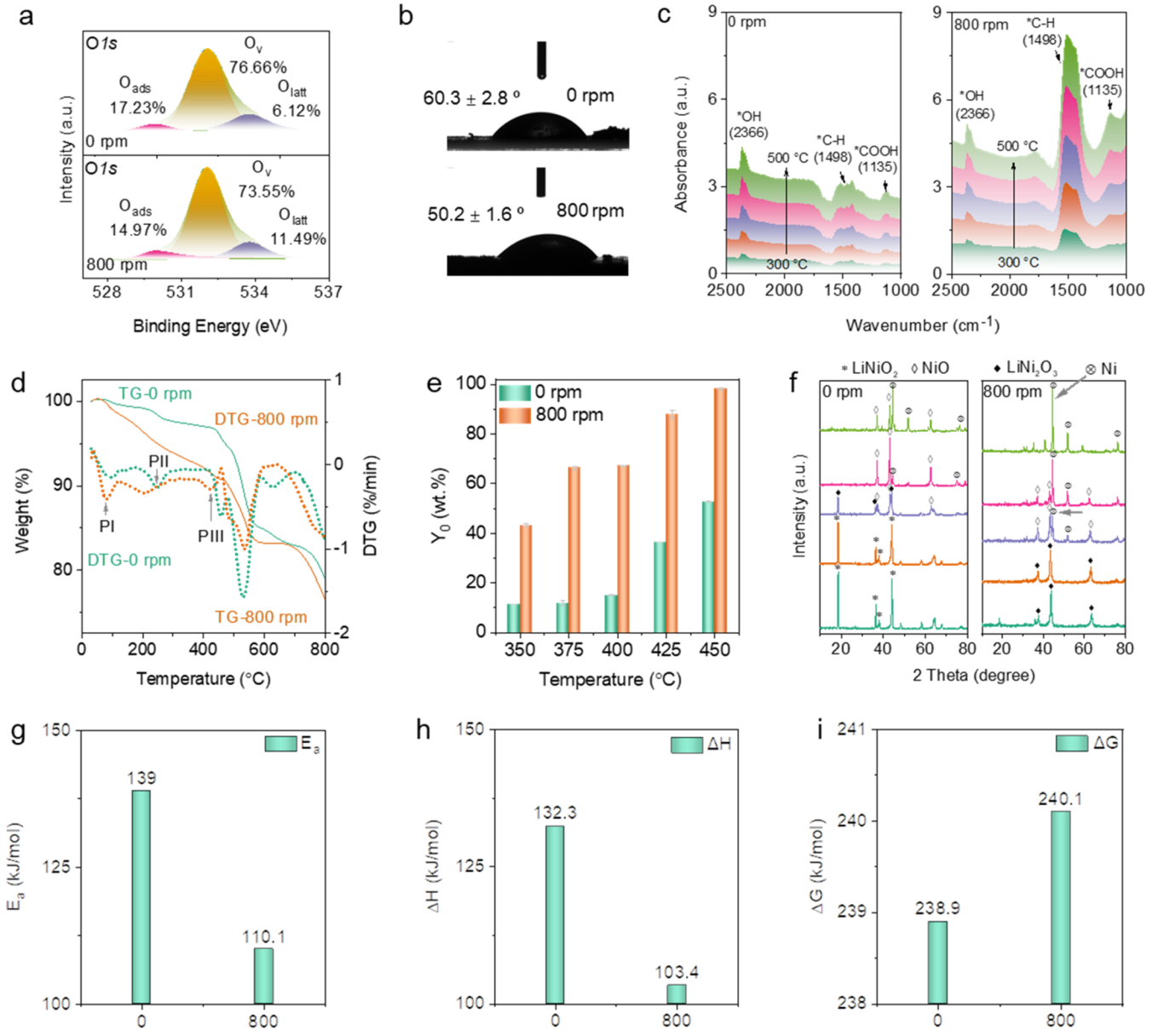

Figure 3. NCM cathode materials: (a) XPS results of O 1s (after mechanochemical processing and H_2 treatment at 450 °C), (b) contact angle test (after mechanochemical processing and H_2 treatment at 450 °C), (c) *in situ* FT-IR spectra (the test interval is 50 °C), (d) TG−DTG curves (H_2 and heating rate of 10 °C/min); (e) leaching efficiency of Li after H_2 treatment at different temperatures (5% (v/v) H_2 gas, with He as the protective gas, and a heating rate of 10 °C/min); (f) XRD patterns of reaction products obtained from H_2 treatment at different temperatures (corresponding to (e), temperatures from bottom to top were 350, 375, 400, 425, and 450 °C, respectively); (g) thermal activation energy, (h) enthalpy change, and (i) Gibbs free energy change of NCM cathode materials fitted by the KAS method.

intensities, i.e., $R = (I_{(006)} + I_{(102)})/I_{(101)}$, demonstrated the transformation of NCM cathode materials from an ordered (1.13) to a disordered state (0.52) following mechanochemical processing.

Before mechanochemical processing, the cell parameters of the spinel phase $LiNiO_2$ (JCPDF: 01−089−3601) obtained by Rietveld refinement of XRD data were a = 2.87 Å, b = 2.87 Å, and c = 14.23 Å (Figure 1e), while they increased slightly to a = 2.88 Å, b = 2.88 Å, and c = 14.25 Å (Figure 1f) after mechanochemical processing, indicating a slight increase in the crystal volume. The SEM images depict the impact of mechanochemical forces such as shear and friction on NCM (Figure 1g). The results from the laser particle size analyzer (Figure S4) show a decrease in average particle size after mechanochemical processing (800 rpm). Additionally, the variations in energy storage of NCM cathode materials were measured using DSC curves. Before mechanochemical processing, the endothermic (ΔH_{endo}) of NCM cathode materials was 16.4 J/g, upon completion of the process, a heat release (ΔH_{exo}) of 3.1 J/g was observed in the DSC curve. These results confirm the grain refinement and lattice distortion in NCM cathode materials, which probably serve as the primary location for internal energy storage (Figure 1h).[41] Overall, mechanochemical processing can promote the refinement of NCM crystal particles, induce lattice disorder, and increase internal energy, thus exposing more reactive sites in the battery materials for subsequent recycling.[38]

https://doi.org/10.1021/acs.est.4c06562
Environ. Sci. Technol. 2024, 58, 21362−21373

3.2. Identification of Oxygen Vacancies and Carbon Defects. We examined changes in the active sites in NCM cathode materials after mechanochemical processing. Structural defects in the NCM cathode materials were analyzed using AC STEM-HAADF (Figure 2a). Point defects and vacancies are widely visible on the crystal surface within the STEM field of view. A significant number of defects are detected in the lattice region, likely due to the formation of atom vacancies in Area 1 and Area 2 (Figure 2b). The TG−DTG analysis showed that compared to the initial state (0 rpm), the weight loss of NCM cathode materials significantly decreased after mechanochemical processing, which may be due to the escape of reactive oxygen species caused by heating (Figure 2c).[42] After mechanochemical processing, EPR revealed an increased O_v signal at g = 2.004, suggesting that mechanical force can disturb the crystal structures of NCM, resulting in the creation of oxygen defects (Figure 2d).[43] The O 1s analysis revealed three categories of oxygen vacancies: O_{latt}, O_v, and O_{ads}. The proportion of O_v on the surface increased from 38.9 to 47.9% following an increase to 800 rpm (Figure 2e). Upon further analysis of Ni 2p, Co 2p, and Mn 2p, it was observed that the ratio of Ni^{2+}/Ni^{3+} increased in the ball-milled NCM cathode materials compared to the original sample. Additionally, distinctive peaks of Co^0 and Mn^0 emerged, indicating that surface reduction of Ni^{2+}, Co^{3+}, and Mn^{4+} was caused by mechanochemical processing (Figure S5).

Oxygen temperature-programmed desorption (O_2-TPD) was employed to determine the oxygen species present within the NCM crystals (Figure 2f).[44] The curve of the unprocessed NCM cathode materials in the visible spectra exhibited distinctive desorption peaks indicative of O^{2-}, O^-, and O_2. Following mechanochemical processing, the desorption peaks shifted significantly to the left, with a 1.6-fold increase in desorption quantity. The desorption peak intensity of O^{2-} at 649.2 °C notably increased, suggesting that oxygen adsorbs at the defect sites of oxygen vacancies and rapidly releases as the temperature rises.[45] The above findings confirm that mechanochemical processing significantly increases the concentration of oxygen vacancies in the NCM cathode materials, which can probably serve as the primary active sites driving the rapid H_2 reduction reaction. The C 1s spectra of NCM cathode materials are displayed in Figure 2g, which are primarily subdivided into three subpeaks corresponding to C−C (sp^2), a "defect peak" (sp^3), and C−O, at 284.8, 285.7, and 288.7 eV, respectively. The 800 rpm-NCM cathode materials showed a notable $\pi-\pi^*$ satellite peak, which verified the appearance of CO_3^{2-} species. The sp^2/sp^3 ratio dropped from 3.85 to 1.33 in the NCM cathode materials before and after mechanochemical processing, suggesting that the C species in the processed NCM cathode materials have more edges and flaws. Furthermore, the I_D/I_G value of graphite (Raman spectra, Figure S6) in the NCM cathode materials decreased from 0.43 to 0.12, indicating that the mechanical forces caused the graphite to transform from a multilayer toward a monolayer.

The above results confirm the crystal structure destabilization of NCM cathode materials to varying degrees, increasing the contents of carbon defects and oxygen vacancies. The H_2-TPR analysis unveiled distinct peaks corresponding to Co^{3+} and Mn^{3+} at 378 and 482 °C, respectively, in the unprocessed cathode materials. In contrast, the processed NCM cathode materials exhibited a significant decrease in the intensities of these peaks, accompanied by the emergence of a Co^{2+}/Co^{3+} peak at 417 °C and a noticeable leftward shift in the Mn^{3+} peak to 481 °C (Figure 2h). The decreased intensity indicates the formation of C_v-O_v on the NCM cathode materials, which may possibly reduce the H_2 consumption in the subsequent recycling process.

3.3. Efficacy of Oxygen Vacancies and Carbon Defects. We examined how $C_v-O_v-H_2$ reduction affects the decomposition of NCM cathode materials. After the H_2 reduction process, a lower O_v content of NCM cathode materials was found after mechanochemical processing (from 76.7 to 73.6%) (Figure 3a). More oxygen vacancies were consumed through the $C_v-O_v-H_2$ strategy. The hydrophilicity of NCM cathode materials increased after mechanochemical processing and H_2 treatment of 450 °C, indicating the formation of more OH groups on the surface of NCM (Figure 3b). We conducted EPR and XPS analyses on the samples subjected to H_2 reduction at 800 rpm to elucidate the relationships between O_v concentration and temperature of H_2 reduction. With the continuous increase of the H_2 reduction temperature, the EPR results confirm a significant decrease in the intensity of O_v, indicating that the H_2 reduction can effectively annihilate the oxygen vacancies in the NCM crystals (Figure S7). The XPS results show that the percentage concentration of O_v continuously decreases as the reduction temperature of H_2 increases (Figure S8), confirming that the thermal reduction can convert the oxygen vacancies on the surface of NCM samples. The H_2 first breaks down to H* on the O_v surface of NCM, which then combines with O species to form −OH (schematic diagram of H_2 decomposition on the surface of NCM cathode materials, Figure S9). Based on the *in situ* FT-IR spectra, the observed peaks were found at the locations of 2366, 1498, and 1135 cm^{-1} (Figure 3c). A *OH functional group or water molecule is shown by the peak at 2366 cm^{-1}, which is probably produced by the H_2 reduction reaction. The signal at 1135 cm^{-1} is associated with carboxylate salts or carboxyl (*COOH) functional groups. The synergistic interactions among C, O species, and H_2 may cause the appearance of these chemical moieties. Following mechanochemical processing, the NCM cathode materials showed a distinct characteristic peak at 1498 cm^{-1} that belongs to *C−H. Mechanochemical processing, which results in the synthesis of alkanes or aromatics through H_2 cracking fueled by faulty carbon species, is responsible for the increase in the abundance of *C−H bonds. As a result, the defective carbon generated by mechanochemical processing can accelerate the H_2 gas cracking reaction.

Figure 3d displays the TG−DSC curves of NCM cathode materials in an H_2 atmosphere. The TG curve reveals a notable increase in the weight loss rate of the NCM cathode materials, suggesting that the presence of oxygen vacancies can accelerate the reduction reaction of NCM cathode materials. The leftward shift of peaks PI, PII, and PIII in the DTG curve indicates a faster elimination rate of oxygen. The ICP-OES results demonstrate a significant increase in Li dissolution into deionized water for the processed samples compared with the unprocessed samples (Figure 3e). The leaching percentage of Li was positively correlated with the rotational speed (Figure S10). The NCM cathode materials after mechanochemical processing exhibit a more noticeable phase transition in the same temperature range, with NiO and elemental Ni peaks emerging more rapidly. At 450 °C, NiO peaks are still visible in the unprocessed sample, whereas NiO vanishes leaving only Ni peaks in the processed sample (Figure 3f). The above results

https://doi.org/10.1021/acs.est.4c06562
Environ. Sci. Technol. 2024, 58, 21362−21373

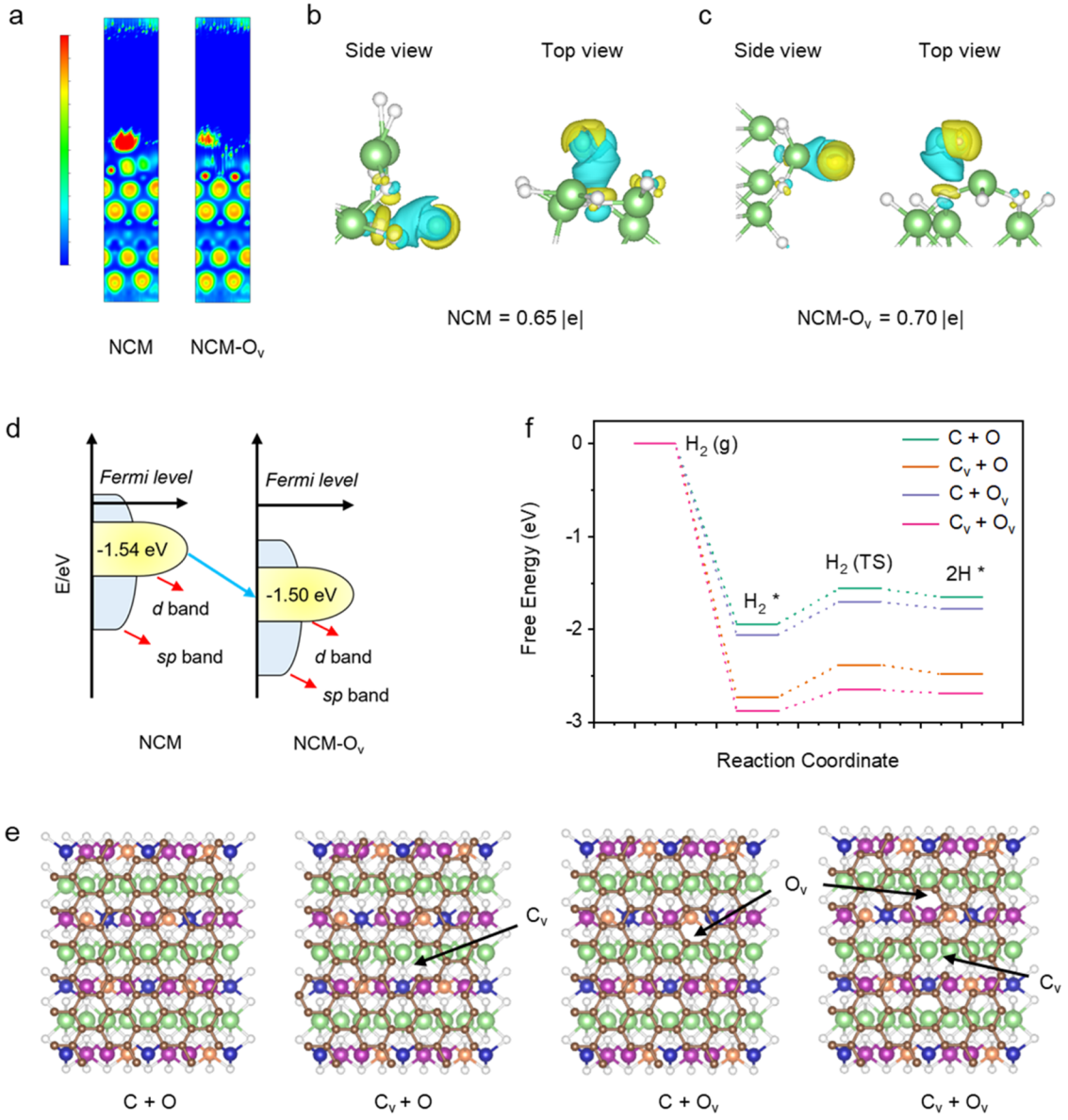

Figure 4. (a) Electronic local function of NCM and NCM-O_v; differential and bard charge results of (b) NCM and (c) NCM-O_v. Yellow represents the accumulation of electron density, while blue represents the consumption of electron density. Among them, white represents O atoms, and green represents Li atoms; (d) calculation results of d-band center.; (e) electronic configurations of C + O, C_v + O, C + O_v, and C_v + O_v, and (f) reaction free energy of different electronic configurations for H_2 cracking (The corresponding relationship between colors and balls is as follows: green = Li, blue = Co, white = O, purple = Mn, orange = Ni, brown = C; view along the *c* axis).

confirm that the increase of oxygen vacancies can promote a faster reduction of processed NCM in the H_2 atmosphere. The reaction pathways of Li, Ni, Co, and Mn were analyzed using Gibbs free energy calculation (Figure S11) and phase diagrams (Figure S12). The changes in Ni, Co, and Mn phases shown by Gibbs free energy analysis and phase diagrams are consistent with the XRD results.

We employed the Kissinger−Akahira−Sunose (KAS) method to determine the activation energy, enthalpy change, and Gibbs free energy of NCM cathode materials at various heating rates. The average activation energy for the NCM sample before and after mechanochemical processing was 139.01 and 110.11 kJ/mol, respectively, indicating a notable reduction in the activation energy for the thermolytic reaction of the processed sample (Figure 3g and Tables S9 and S10 are the corresponding fitting data). The enthalpy change (ΔH) of a chemical reaction is the energy difference involved in the reaction process. The positive ΔH values from the calculation suggest that the H_2 reduction thermolysis of NCM is an endothermic process. The reduction in ΔH (from 132.3 to 103.4 kJ/mol) suggests that mechanochemical processing is beneficial for producing thermolytic products (Figure 3h and Tables S9 and S10). The Gibbs free energy is the change in system energy as the NCM sample creates an activated complex, indicating the remaining energy accessible to the system. The ΔG values for the NCM samples before and after mechanochemical processing are 238.9 and 240.1 kJ/mol, respectively, suggesting that activation has a minimal effect on the energy acquired by the system (Figure 3i). Based on the Coats−Redfern method, the kinetic parameter of the H_2 reduction reaction is $(1 - \alpha)$ before mechanochemical processing, which belongs to random nucleation (first order)

https://doi.org/10.1021/acs.est.4c06562
Environ. Sci. Technol. 2024, 58, 21362−21373

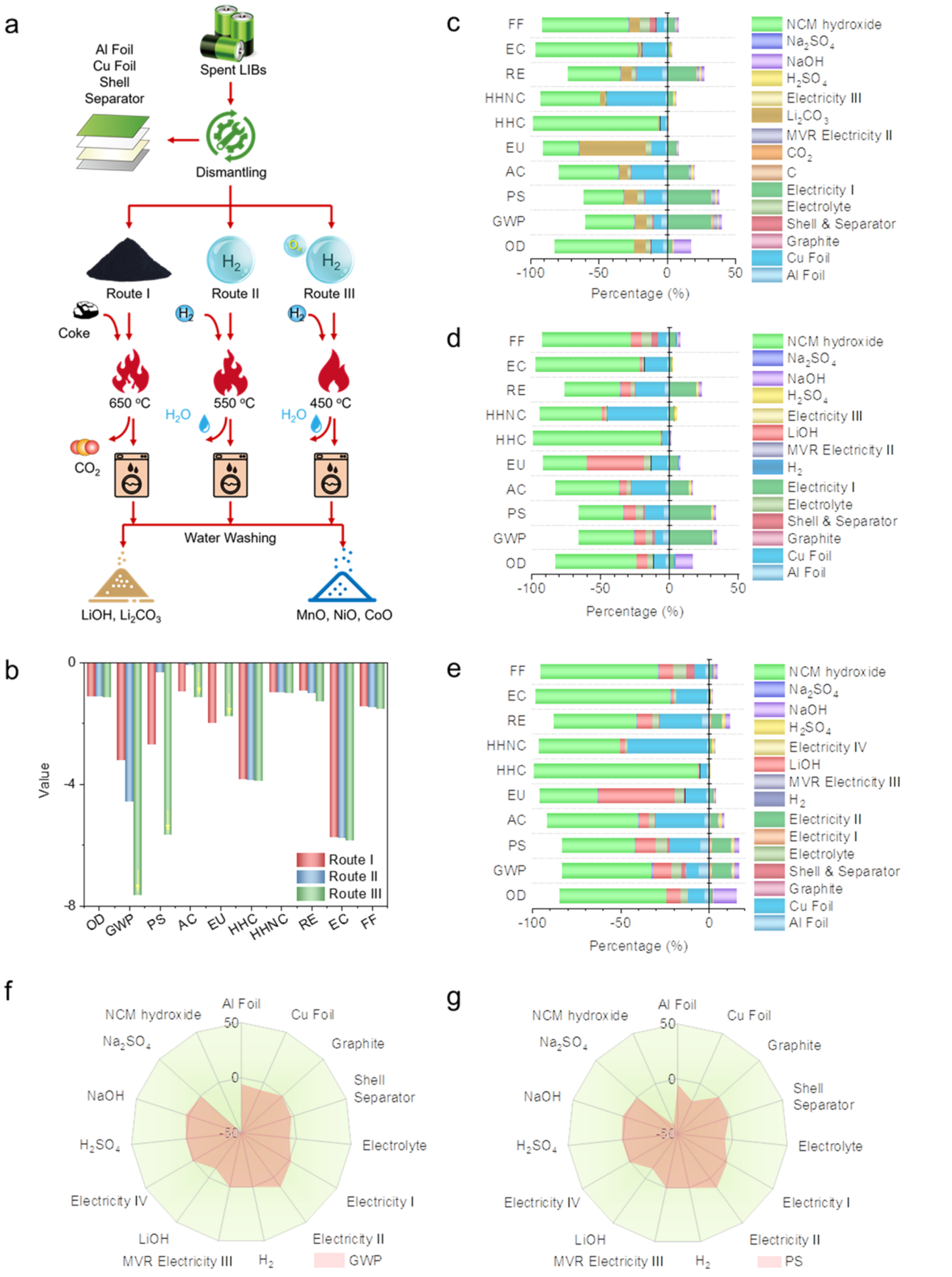

Figure 5. (a) Process diagrams of three NCM cathode material recovery routes (Route I: C based metallurgical processing, Route II: H_2 reduction metallurgical processing, and Route III: $C_v-O_v-H_2$ reduction metallurgical processing), (b) quantitative comparison results of different NCM cathode material recovery routes; percentage of full life cycle assessment for different NCM cathode material recovery routes include (c) C based

https://doi.org/10.1021/acs.est.4c06562
Environ. Sci. Technol. 2024, 58, 21362−21373

Figure 5. continued

metallurgical processing, (d) H_2 reduction metallurgical processing, and (e) $C_v-O_v-H_2$ reduction metallurgical processing; percentage contribution of different materials and energy sources to (f) GWP, and (g) PS indicators.

with one nucleus per particle. After mechanochemical processing, the kinetic parameter changes to $3(1-\alpha)^{2/3} \times [2(1-(1-\alpha)^{1/3})]^{-1}$, which belongs to 3D diffusion (Jander's equation) Table S11 presents the computational model employed in the Coats-Redfern methodology, while Tables S12 and S13 illustrate the mechanism functions and outcomes for the tested samples, respectively.

3.4. Theoretical Calculation of Collaborative Reaction Pathways. DFT calculation was performed to demonstrate the pathway contribution of oxygen vacancies and carbon defects to the accelerated H_2 reduction of NCM cathode materials (Figure S13). The electronic local function analysis (Figure 4a) reveals that the NCM-O_v sample exhibits a greater number of blue regions between H_2 and the transition metal−O region. The electrons are highly delocalized, with blue indicating delocalization and red indicating localization. This suggests a robust interaction between the two regions, which promotes the adsorption and decomposition of H_2. Figure 4b,c illustrate the differential charge distribution along the *ac* axis for NCM and NCM-O_v, respectively, showing a larger relative amount of blue to yellow in the NCM cathode materials, suggesting greater electron charge transfer in NCM-O_v. The blue part is more adsorbed by the NCM cathode materials and is difficult to decompose, consistent with the insight that H_2 is relatively more difficult to decompose on the surface of NCM. The d-band center in NCM-O_v exhibits a downward displacement when compared to NCM (Figure 4d). The observed displacement of the d-band center suggests a notable reduction in the adsorption energy of H_2 intermediates, hence promoting the desorption of H_2 and the subsequent exposure of active sites. Four electronic configurations of C + O, C_v + O, C + O_v, and C_v + O_v were constructed to calculate the cleavage energy of H_2 on their surfaces (Figure 4e). Figure 4f displays the H_2 activation energy barriers. NCM cathode materials, after the formation of C_v + O_v, have a lower free energy, indicating that the synergistic effect of C_v + O_v is more conducive to the H_2 decomposition compared to C + O, C_v + O, C + O_v, and C_v + O_v. Thus, the carbon defects and oxygen vacancies created in the NCM cathode materials can increase the crystal activity and lower the energy barrier for the H_2 reaction, thereby accelerating the metallurgical decomposition of NCM *via* H_2 reduction.

3.5. Environmental Benefits of $C_v-O_v-H_2$ Processing. In the life cycle assessment for recycling the retired LIBs, three reaction pathways were identified: C-based metallurgical processing (Route I), H_2-reduction metallurgical processing (Route II), and $C_v-O_v-H_2$ reduction metallurgical processing (Route III) (Figure 5a). The thermal decomposition of NCM cathode materials typically necessitates the presence of coke as a reducing agent at 650 °C, which results in significant CO_2 emissions. In the H_2 metallurgical processing route, the elimination of oxygen atoms in NCM produces water vapor without emitting CO_2, and the thermal reduction decomposition of NCM can occur at 550 °C. In comparison, our proposed $C_v-O_v-H_2$ metallurgical processing route design, despite consuming some mechanical energy, can greatly decrease the energy usage in the NCM thermal decomposition process at 450 °C. The results of OD, HHC, HHNC, RE, EC, and FF show comparable environmental effects, suggesting that the $C_v-O_v-H_2$ reduction metallurgical process did not influence these environmental burdens (Figure 5b). Moreover, the results of GWP, PS, AC, and EU demonstrate greater environmental advantages for the $C_v-O_v-H_2$ metallurgical processing route. For instance, the GWP values for recovering 1.0 kg of spent LIBs from Routes I, II, and III were −3.23, −4.58, and −7.65 kg CO_2 eq, respectively. The results and discussion of GWP analysis for carbon emissions are supplemented in Table S14. Thus, the $C_v-O_v-H_2$ processing can significantly reduce global carbon emissions.

The percentages of various materials and energy contributions to environmental impacts in the LCA of the three proposed routes are shown in Figure 5c−e. None of the three routes showed any negative environmental impacts. NCM precursors and Li oxides had the most significant positive environmental impact, whereas copper foil and aluminum foil had lesser benefits. Recycled products can serve as substitutes for comparable items in the market, thereby lowering the release of environmental pollutants during mining/extraction and manufacturing. Comparing Figure 5d,e, a clear shift to the right of the *y*-axis at zero indicates that the synergistic integration of C_v-O_v can enhance the environmental advantages of H_2 reduction metallurgical processing. We analyzed the contribution percentages of various materials and energy in the GWP and PS indicators in Figure 5f,g. The radar chart trend effectively demonstrates that energy consumption, specifically Electricity I, Electricity II, and NaOH, remained the most probable risk factors that could harm the environment.

The examination of the technical advantages indicated that the $C_v-O_v-H_2$ reduction process via mechanochemical activation is capable of fully leveraging the intrinsic graphite present in the cathode electrode materials and markedly decreasing the temperature required for direct H_2 reduction (as shown in Table S15). This study presents a synergistic integration of C_v-O_v in the context of the thermal decomposition of spent LIBs. Technological progress in this study presents a significant potential for scalable applications and warrants further research.

4. ENVIRONMENTAL IMPLICATIONS

Sustainable development of the global electric vehicle industry relies on the low-carbon recycling of retired LIBs. Eco-friendly and efficient deconstruction strategy of active crystals in cathode materials is crucial for closing the loop on technology-critical metals for LIBs, which requires our holistic understanding about the material/energy input of pyrometallurgical recovery systems to ensure the overall sustainability with technological, economic, and environmental advantages. We suggest utilizing a metallurgical approach that leverages C_v-O_v generation to disassemble the retired LIB cathode materials at lower temperatures. Following mechanochemical processing and H_2 reduction, NCM cathode materials can rapidly decompose at 450 °C, resulting in the selective removal of Li and carbon-free decomposition of active crystals. The introduction of C_v and O_v is proven to improve the charge

https://doi.org/10.1021/acs.est.4c06562
Environ. Sci. Technol. 2024, 58, 21362−21373

transfer of H_2 with NCM cathode materials and lower the energy barrier for reduction reactions. Our proposed C_v−O_v−H_2 reduction processing can reduce CO_2 emissions by 4.42 kg CO_2 eq of recycling 1.0 kg retired LIBs, thus promoting the low-carbon recycling of technology-critical metals compared to conventional approaches. This work advances our mechanistic knowledge for reducing carbon footprints and pollutant emissions during the recycling process of retired battery materials, which has significant environmental and industrial benefits for fostering a circular economy.

■ ASSOCIATED CONTENT

Supporting Information

The Supporting Information is available free of charge at https://pubs.acs.org/doi/10.1021/acs.est.4c06562.

Dismantling of spent $LiNi_{0.5}Co_{0.2}Mn_{0.3}O_2$ battery (Note S1); element mass percentages of cathode material in $LiNi_{0.5}Co_{0.2}Mn_{0.3}O_2$ battery (Note S2); pyrolysis kinetics and thermodynamics evaluation (Note S3); LCA calculation details for spent $LiNi_{0.5}Co_{0.2}Mn_{0.3}O_2$ battery recovery using the carbon metallurgical process (Note S4); LCA calculation details of spent $LiNi_{0.5}Co_{0.2}Mn_{0.3}O_2$ battery recovery by the hydrogen reduction metallurgical process (Note S5); LCA calculation details of spent $LiNi_{0.5}Co_{0.2}Mn_{0.3}O_2$ battery recovery by C_v−O_v−H_2 metallurgical process (Note S6); System boundaries for recycling 1.0 kg spent $LiNi_{0.5}Co_{0.2}Mn_{0.3}O_2$ battery by carbon metallurgical process (Figure S1); system boundaries for recycling 1.0 kg spent $LiNi_{0.5}Co_{0.2}Mn_{0.3}O_2$ battery by hydrogen metallurgical process (Figure S2); system boundaries for recycling 1.0 kg spent $LiNi_{0.5}Co_{0.2}Mn_{0.3}O_2$ battery by oxygen vacancy and hydrogen metallurgical process (Figure S3); particle size distribution of 0 and 800 rpm samples (Figure S4); XPS results of (a) Ni, (b) Co, and (c) Mn before and after mechanochemical processing (Figure S5); Raman spectra of NCM cathode materials before and after mechanochemical processing (Figure S6); EPR results of 800 rpm samples after H_2 reduction reaction (Figure S7); O 1s XPS results of NCM-800 rpm samples after H_2 reduction reaction (Figure S8); reaction pathway of H_2 on the O_v surface (Figure S9); leaching percentage of Li under different mechanochemical processing speeds (Figure S10); Gibbs free energy for the reaction pathways of Li, Ni, Co, and Mn (Figure S11); phase diagrams of Li, Ni, Co, and Mn (Figure S12); (a) formation energy of O_v in NCM, PDOS results of O in (b) NCM and (c) NCM-O_v; (d) reaction free energy of NCM and NCM-O_v (Figure S13); weight proportion of each part of the spent $LiNi_{0.5}Co_{0.2}Mn_{0.3}O_2$ battery (Table S1); element mass percentages of the cathode material in $LiNi_{0.5}Co_{0.2}Mn_{0.3}O_2$ battery (Table S2); LCA data inventory for spent $LiNi_{0.5}Co_{0.2}Mn_{0.3}O_2$ battery recovery by carbon metallurgical process (Table S3); LCA data inventory for spent $LiNi_{0.5}Co_{0.2}Mn_{0.3}O_2$ battery recovery by hydrogen metallurgical process (Table S4); LCA data inventory for spent $LiNi_{0.5}Co_{0.2}Mn_{0.3}O_2$ battery recovery by oxygen vacancy and hydrogen metallurgical process (Table S5); LCA data source of spent $LiNi_{0.5}Co_{0.2}Mn_{0.3}O_2$ battery recovery by carbon metallurgical process (Table S6); LCA data source of spent $LiNi_{0.5}Co_{0.2}Mn_{0.3}O_2$ battery recovery by hydrogen metallurgical process (Table S7); LCA data source of spent $LiNi_{0.5}Co_{0.2}Mn_{0.3}O_2$ battery recovery by oxygen vacancy and hydrogen metallurgical process (Table S8); activation energy calculated using the KAS method along with fitted equations and correlation coefficients for both 0 and 800 rpm samples (Table S9); pre-exponential parameters and thermodynamic parameters evaluated at 10 °C/min heating rates for 0 and 800 rpm samples (Table S10); $F(\alpha)$ and $g(\alpha)$ mechanism functions of pyrolysis kinetics (Table S11); mechanism functions of pyrolysis kinetics of 0 rpm sample (Table S12); mechanism functions of pyrolysis kinetics of 800 rpm sample (Table S13); GWP analysis of different retired NCM battery recycling routes (Table S14), and literature summary on thermal decomposition of spent lithium-ion battery cathode materials (Table S15) (PDF)

■ AUTHOR INFORMATION

Corresponding Author

Daniel C. W. Tsang − *Department of Civil and Environmental Engineering, The Hong Kong University of Science and Technology, Hong Kong 999077, China;* orcid.org/0000-0002-6850-733X; Email: cedan@ust.hk

Authors

Kang Liu − *Department of Civil and Environmental Engineering, The Hong Kong University of Science and Technology, Hong Kong 999077, China*

Zibo Xu − *Department of Civil and Environmental Engineering, The Hong Kong University of Science and Technology, Hong Kong 999077, China*

Mengmeng Wang − *Department of Civil and Environmental Engineering, The Hong Kong University of Science and Technology, Hong Kong 999077, China*

Daniel S. Alessi − *Department of Earth and Atmospheric Sciences, University of Alberta, Edmonton, Alberta T6G 2R3, Canada;* orcid.org/0000-0002-8360-8251

Yuanzhi Tang − *School of Earth and Atmospheric Sciences, Georgia Institute of Technology, Atlanta, Georgia 30332, United States;* orcid.org/0000-0002-7741-8646

Complete contact information is available at: https://pubs.acs.org/10.1021/acs.est.4c06562

Notes

The authors declare no competing financial interest.

■ ACKNOWLEDGMENTS

The authors appreciate the financial support from the Hong Kong Research Grants Council (HKUST 15231522), Hong Kong RGC Postdoctoral Fellowship Scheme, and HKUST "30 for 30" Talent Acquisition Campaign.

■ REFERENCES

(1) Manthiram, A. A reflection on lithium-ion battery cathode chemistry. *Nat. Commun.* **2020**, *11* (1), No. 1550.

(2) Armand, M.; Axmann, P.; Bresser, D.; Copley, M.; Edström, K.; Ekberg, C.; Guyomard, D.; Lestriez, B.; Novák, P.; Petranikova, M.; et al. Lithium-ion batteries−Current state of the art and anticipated developments. *J. Power Sources* **2020**, *479*, No. 228708.

(3) Masias, A.; Marcicki, J.; Paxton, W. A. Opportunities and challenges of lithium ion batteries in automotive applications. *ACS Energy Lett.* **2021**, *6* (2), 621−630.

(4) Deng, J.; Bae, C.; Denlinger, A.; Miller, T. Electric vehicles batteries: requirements and challenges. *Joule* **2020**, *4* (3), 511−515.
(5) Miao, Y.; Liu, L.; Zhang, Y.; Tan, Q.; Li, J. An overview of global power lithium-ion batteries and associated critical metal recycling. *J. Hazard. Mater.* **2022**, *425*, No. 127900.
(6) Sun, X.; Liu, Z.; Zhao, F.; Hao, H. Global competition in the lithium-ion battery supply chain: a novel perspective for criticality analysis. *Environ. Sci. Technol.* **2021**, *55* (18), 12180−12190.
(7) Makuza, B.; Tian, Q.; Guo, X.; Chattopadhyay, K.; Yu, D. J. J. o. P. S. Pyrometallurgical options for recycling spent lithium-ion batteries: A comprehensive review. *J. Power Sources* **2021**, *491*, No. 229622.
(8) Liu, K.; Tan, Q.; Yu, J.; Wang, M. A global perspective on e-waste recycling. *Circ. Econ.* **2023**, *2* (1), No. 100028.
(9) Liang, Z.; Cai, C.; Peng, G.; Hu, J.; Hou, H.; Liu, B.; Liang, S.; Xiao, K.; Yuan, S.; Yang, J. J. A. S. C. Engineering, Hydrometallurgical recovery of spent lithium ion batteries: environmental strategies and sustainability evaluation. *ACS Sustainable Chem. Eng.* **2021**, *9* (17), 5750−5767.
(10) Jenis, P.; Zhang, T.; Ramasubramanian, B.; Lin, S.; Rayavarapu, P. R.; Yu, J.; Ramakrishna, S. Recent progress and hurdles in cathode recycling for Li-ion batteries. *Circ. Econ.* **2024**, *3* (2), No. 100087.
(11) Wu, J.; Zheng, M.; Liu, T.; Wang, Y.; Liu, Y.; Nai, J.; Zhang, L.; Zhang, S.; Tao, X. J. E. S. M. Direct recovery: A sustainable recycling technology for spent lithium-ion battery. *Energy Storage Mater.* **2023**, *54*, 120−134.
(12) Kaya, M. State-of-the-art lithium-ion battery recycling technologies. *Circ. Econ.* **2022**, *1* (2), No. 100015.
(13) Du, K.; Ang, E. H.; Wu, X.; Liu, Y. Progresses in sustainable recycling technology of spent lithium-ion batteries. *Energy Environ. Mater.* **2022**, *5* (4), 1012−1036.
(14) Li, Y.; Lv, W.; Huang, H.; Yan, W.; Li, X.; Ning, P.; Cao, H.; Sun, Z. J. G. C. Recycling of spent lithium-ion batteries in view of green chemistry. *Green Chem.* **2021**, *23* (17), 6139−6171.
(15) Zeng, X.; Ogunseitan, O. A.; Nakamura, S.; Suh, S.; Kral, U.; Li, J.; Geng, Y. Reshaping global policies for circular economy. *Circ. Econ.* **2022**, *1* (1), No. 100003.
(16) Singh, N.; Ogunseitan, O. A. Disentangling the worldwide web of e-waste and climate change co-benefits. *Circ. Econ.* **2022**, *1* (2), No. 100011.
(17) Makuza, B.; Tian, Q.; Guo, X.; Chattopadhyay, K.; Yu, D. Pyrometallurgical options for recycling spent lithium-ion batteries: A comprehensive review. *J. Power Sources* **2021**, *491*, No. 229622.
(18) Hantanasirisakul, K.; Sawangphruk, M. Sustainable Reuse and Recycling of Spent Li-Ion batteries from Electric Vehicles: Chemical, Environmental, and Economical Perspectives. *Global Challenges* **2023**, *7* (4), No. 2200212.
(19) Xiao, J.; Li, J.; Xu, Z. Novel approach for in situ recovery of lithium carbonate from spent lithium ion batteries using vacuum metallurgy. *Environ. Sci. Technol.* **2017**, *51* (20), 11960−11966.
(20) Xiao, J.; Li, J.; Xu, Z. Challenges to future development of spent lithium ion batteries recovery from environmental and technological perspectives. *Environ. Sci. Technol.* **2020**, *54* (1), 9−25.
(21) Men, L.; Feng, S.; Zhang, J.; Luo, X.; Zhou, Y. A systematic review of efficient recycling for cathode materials of spent lithium-ion batteries: process intensification technologies beyond traditional methods. *Green Chem.* **2024**, *26*, 1170−1193.
(22) Xiao, X.; Wang, L.; Wu, Y.; Song, Y.; Chen, Z.; He, X. Cathode regeneration and upcycling of spent LIBs: toward sustainability. *Energy Environ. Sci.* **2023**, *16* (7), 2856−2868.
(23) Castro, F. D.; Vaccari, M.; Cutaia, L. Valorization of resources from end-of-life lithium-ion batteries: A review. *Crit. Rev. Environ. Sci. Technol.* **2022**, *52* (12), 2060−2103.
(24) Gutsch, M.; Leker, J. Costs, carbon footprint, and environmental impacts of lithium-ion batteries−From cathode active material synthesis to cell manufacturing and recycling. *Appl. Energy* **2024**, *353*, No. 122132.
(25) Li, J.; Xu, G. Circular economy towards zero waste and decarbonization. *Circ. Econ.* **2022**, *1* (1), No. 100002, DOI: 10.1016/j.cec.2022.100002.
(26) Chen, Q.; Lai, X.; Gu, H.; Tang, X.; Gao, F.; Han, X.; Zheng, Y. J. J. o. C. P. Investigating carbon footprint and carbon reduction potential using a cradle-to-cradle LCA approach on lithium-ion batteries for electric vehicles in China. *J. Cleaner Prod.* **2022**, *369*, No. 133342.
(27) Tong, Y.; Qin, C.; Zhu, L.; Chen, S.; Lv, Z.; Ran, J. J. E. S. Technology, From spent lithium-ion batteries to low-cost Li_4SiO_4 sorbent for CO_2 capture. *Environ. Sci. Technol.* **2022**, *56* (9), 5734−5742.
(28) Wang, J.; Ma, J.; Zhuang, Z.; Liang, Z.; Jia, K.; Ji, G.; Zhou, G.; Cheng, H.-M. J. C. R. Toward Direct Regeneration of Spent Lithium-Ion Batteries: A Next-Generation Recycling Method. *Chem. Rev.* **2024**, *124* (5), 2839−2887.
(29) Zhang, X.; Li, L.; Fan, E.; Xue, Q.; Bian, Y.; Wu, F.; Chen, R. J. C. S. R. Toward sustainable and systematic recycling of spent rechargeable batteries. *Chem. Soc. Rev.* **2018**, *47* (19), 7239−7302.
(30) Hafner, J. Ab-initio simulations of materials using VASP: Density-functional theory and beyond. *J. Comput. Chem.* **2008**, *29* (13), 2044−2078.
(31) Blöchl, P. E. Projector augmented-wave method. *Phys. Rev. B* **1994**, *50* (24), No. 17953.
(32) Gajdoš, M.; Hummer, K.; Kresse, G.; Furthmüller, J.; Bechstedt, F. Linear optical properties in the projector-augmented wave methodology. *Phys. Rev. B* **2006**, *73* (4), No. 045112.
(33) Enkovaara, J.; Rostgaard, C.; Mortensen, J. J.; Chen, J.; Dułak, M.; Ferrighi, L.; Gavnholt, J.; Glinsvad, C.; Haikola, V.; Hansen, H.; et al. Electronic structure calculations with GPAW: a real-space implementation of the projector augmented-wave method. *J. Phys.: Condens. Matter* **2010**, *22* (25), No. 253202.
(34) Perdew, J. P.; Burke, K.; Ernzerhof, M. Generalized gradient approximation made simple. *Phys. Rev. Lett.* **1996**, *77* (18), No. 3865.
(35) Wu, F.; Zhou, Z.; Hicks, A. L. Life cycle impact of titanium dioxide nanoparticle synthesis through physical, chemical, and biological routes. *Environ. Sci. Technol.* **2019**, *53* (8), 4078−4087.
(36) An, J.; Wu, F.; Wang, D.; You, J. Estimated material metabolism and life cycle greenhouse gas emission of major plastics in China: A commercial sector-scale perspective. *Resour., Conserv. Recycl.* **2022**, *180*, No. 106161.
(37) Wu, F.; Zhou, Z.; Temizel-Sekeryan, S.; Ghamkhar, R.; Hicks, A. L. Assessing the environmental impact and payback of carbon nanotube supported CO_2 capture technologies using LCA methodology. *J. Cleaner Prod.* **2020**, *270*, No. 122465.
(38) Wang, M.; Liu, K.; Yu, J.; Zhang, C.-C.; Zhang, Z.; Tan, Q. Recycling spent lithium-ion batteries using a mechanochemical approach. *Circ. Econ.* **2022**, *1* (2), No. 100012.
(39) Wang, M.; Tan, Q.; Li, J. Unveiling the role and mechanism of mechanochemical activation on lithium cobalt oxide powders from spent lithium-ion batteries. *Environ. Sci. Technol.* **2018**, *52* (22), 13136−13143.
(40) Yu, Z.; Qu, X.; Wan, T.; Dou, A.; Zhou, Y.; Peng, X.; Su, M.; Liu, Y.; Chu, D. Synthesis and mechanism of high structural stability of nickel-rich cathode materials by adjusting Li-excess. *ACS Appl. Mater. Interfaces* **2020**, *12* (36), 40393−40403.
(41) Zhang, Y.-h.; Wei, X.; Gao, J.-l.; Hu, F.; Qi, Y.; Zhao, D.-l. Electrochemical hydrogen storage behaviors of as-milled Mg−Ti−Ni−Co−Al-based alloys applied to Ni-MH battery. *Electrochim. Acta* **2020**, *342*, No. 136123.
(42) Ndayiragije, S.; Zhang, Y.; Zhou, Y.; Song, Z.; Wang, N.; Majima, T.; Zhu, L. Mechanochemically tailoring oxygen vacancies of MnO_2 for efficient degradation of tetrabromobisphenol A with peroxymonosulfate. *Appl. Catal., B* **2022**, *307*, No. 121168.
(43) Qin, Q.; Liu, T.; Zhang, J.; Wei, R.; You, S.; Xu, Y. Facile synthesis of oxygen vacancies enriched α-Fe2O3 for peroxymonosulfate activation: a non-radical process for sulfamethoxazole degradation. *J. Hazard. Mater.* **2021**, *419*, No. 126447.

(44) Liu, Y.; Zheng, Y.; Feng, D.; Zhang, L.; Zhang, L.; Song, X.; Qiao, Z. A. Efficient Selective Oxidation of Aromatic Alkanes by Double Cobalt Active Sites over Oxygen Vacancy-rich Mesoporous Co_3O_4. *Angew. Chem.* **2023**, *135* (29), No. e202306261.
(45) Yang, Z.; Shi, Y.; Li, H.; Mao, C.; Wang, X.; Liu, X.; Liu, X.; Zhang, L. Oxygen and chlorine dual vacancies enable photocatalytic O_2 dissociation into monatomic reactive oxygen on BiOCl for refractory aromatic pollutant removal. *Environ. Sci. Technol.* **2022**, *56* (6), 3587−3595.

https://doi.org/10.1021/acs.est.4c06562
Environ. Sci. Technol. 2024, 58, 21362−21373